IEEE Access
Multidisciplinary | Rapid Review | Open Access Journal

Received September 12, 2020, accepted September 24, 2020, date of publication September 30, 2020,
date of current version October 13, 2020.

Digital Object Identifier 10.1109/ACCESS.2020.3027844

Reduction of Half-Arm Current Stresses and Flying-Capacitor Voltage Ripples of Flying-Capacitor MMCs

DUC DUNG LE, (Student Member, IEEE), AND DONG-CHOON LEE, (Senior Member, IEEE)
Department of Electrical Engineering, Yeungnam University, Gyeongbuk 38541, South Korea

Corresponding author: Dong-Choon Lee (dclee@yu.ac.kr)

This work was supported by the Korea Institute of Energy Technology Evaluation and Planning (KETEP) and the Ministry of Trade, Industry & Energy (MOTIE) of the Republic of Korea (No. 20194030202310).

ABSTRACT In this paper, a new control scheme that can reduce the current stresses on switching devices, flying capacitors, and inductors for flying-capacitor modular multilevel converters (FC-MMCs) is proposed, which is based on redistribution of power difference between upper and lower arms through the flying capacitors. In addition, a way to determine the frequency range of the square-wave voltage to be injected into the FC-MMC is suggested, which is able to improve the current control performance and reduce the flying-capacitor voltage ripples. The effectiveness of the proposed control scheme has been verified for a 4160-V/1-MW simulation model and a 230-V/3-kW prototype of the FC-MMC.

INDEX TERMS Arm current, medium-voltage motor drive, modular multilevel converters (MMC), submodule (SM) capacitor voltage ripple.

I. INTRODUCTION

Modular multilevel converters (MMCs) feature scalability, modularity, low-distortion output voltages, and fault-tolerant ability. Thus, they have been used in medium to high-voltage applications, such as high-voltage direct-current (HVDC) transmission systems [1]–[5], motor drives [6]–[9], and static synchronous compensators (STATCOMs) [10], [11]. However, one of the main challenges of MMCs for medium-voltage motor drive systems is that the ripple of the submodule (SM) capacitor voltages is proportional to the output current level and inversely proportional to the fundamental frequency [6], [12], [13]. Thus, the voltage ripple becomes larger in lower-speed operation of motor drives, especially in the start-up process. Several empirical studies have been performed to overcome this issue in standstill/low-speed operation.

Several control strategies have been introduced to reduce the level of capacitor voltage ripples in low-speed operation [14]–[23] [24]–[26]. The high-frequency common-mode voltage (CMV) and circulating current have been injected into the three-phase legs of MMCs, which can mitigate SM capacitor voltage ripples. However, the CMV exists on the motor side, which leads to premature failure of the winding insulation and motor bearing [17], [18].

Effective control schemes have been presented to reduce an average voltage of SM capacitor for the conventional MMC [19]–[21], where a higher SM capacitor voltage ripple is allowed without exceeding the maximum voltage of capacitor. According to operating speed regions, whether the high-frequency CMV and circulating current are injected or not is determined. In the high-speed region, any oscillating components into the circulating current are not injected; therefore, the current stresses on switching devices and power losses of the system can be reduced [20]. In the intermediate-speed and low-speed/standstill regions, the high-frequency components are injected [21], and resultantly, the CMV is imposed on the motor winding. In addition, all available voltage for injecting the CMV in an arm can be utilized to minimize the amplitude of circulating current, which results in a reduction of the capacitor size. In [22], the SM capacitor voltage ripple is controlled within a certain range instead of full suppression, which leads to the reduction of the amplitude of circulating current. In the converter design, the SM capacitor with a minimum capacitance can be utilized to minimize the dimension of converters; however, the amplitude

The associate editor coordinating the review of this manuscript and approving it for publication was Chandan Kumar.

of injected components become larger. Therefore, there is a tradeoff between converter efficiency and capacitor.

MMC topologies with auxiliary circuits or additional components have been introduced to suppress the SM capacitor voltage ripples without injecting the CMV [23]–[25]. Cascaded full-bridge submodules (FBSMs) were inserted in each phase on the AC output side of the converter, so the CMV is imposed intentionally on the cascaded FBSMs instead of the motor [23]. However, the cascaded FBMSs increase both the cost and volume of the system.

A new topology of the FC-MMC has been proposed in [24], where a flying capacitor is connected between the middle taps of the upper and lower arms in a leg, which alleviates the SM capacitor voltage ripple without injecting the CMV. However, high-frequency voltage is injected in a sinusoidal waveform, which leads to high peak currents on switching devices, inductors, and flying capacitors, as well as high voltage ripples on flying capacitors. Instead of sinusoidal waveform, a square-wave high-frequency voltage has been injected to reduce the peak value of the current [26]. In this test, the current stresses on the switching devices and flying capacitors can be reduced by 25% and 45%, respectively, where only RL loads were applied to the low-frequency operation of the FC-MMC. Furthermore, no discussion was provided on the determination of the injected frequency range.

In this paper, how to determine the frequency range of the square-wave voltage to be injected into the half-arms of the FC-MMC is proposed, which is important to acquire the reference of AC-circulating current and to reduce the flying-capacitor voltage ripples. In addition, an adjustment scheme of power redistribution through the flying-capacitor branch is suggested in order to reduce the current stresses on switching devices, inductors and flying capacitors. The feasibility of the proposed method is verified for a 4160-V/1-MW simulation model and a 230-V/3-kW prototype of the FC-MMC.

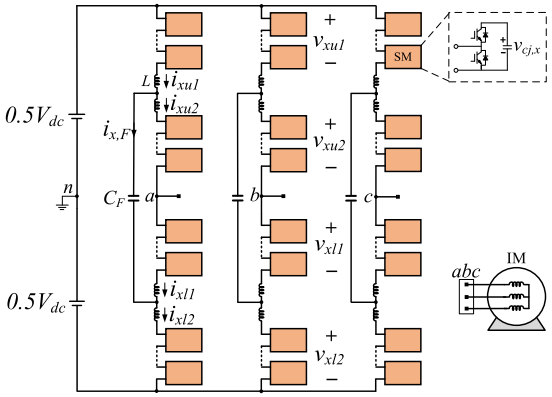

FIGURE 1. Circuit configuration of the FC-MMC.

II. ANALYSIS OF THE FC-MMC UNDER LOW-FREQUENCY OPERATION

A. CIRCUIT CONFIGURATION

Fig. 1 shows the circuit configuration of the FC-MMC, where a leg is composed of two arms, and an arm is divided into two half-arms. A half-arm has $0.5N$ half-bridge SMs (N is the number of half-bridge SMs per arm). The inductor, L, is used in a half-arm to prevent high di/dt. Flying capacitors, C_F, are connected between the middle taps of the upper and lower arms in the three-phase legs (x : a, b, c). The flying capacitance is:

$$C_F = \frac{1}{(2\pi f_r)^2 L}, \tag{1}$$

where f_r is a resonant frequency to reduce the impedance of the equivalent LC circuit.

B. MITIGATION OF SM CAPACITOR VOLTAGE RIPPLE UNDER LOW-SPEED OPERATION

In FC-MMC, the half-arm voltages (v_{xu1}, v_{xu2}, v_{xl1}, and v_{xl2}) in the upper and lower arms are expressed as [24]:

$$v_{xu2} = 0.25V_{dc} - 0.5v_{xs} + v_r, \tag{2}$$
$$v_{xu2} = 0.25V_{dc} - 0.5v_{xs} + v_r, \tag{3}$$
$$v_{xl1} = 0.25V_{dc} + 0.5v_{xs} - v_r, \tag{4}$$
$$v_{xl2} = 0.25V_{dc} + 0.5v_{xs} + v_r, \tag{5}$$

where V_{dc}, v_{xs}, and v_r are the DC-link voltage, AC output voltage, and resonant-frequency voltage, respectively. The half-arm currents (i_{xu1}, i_{xu2}, i_{xl1} and i_{xl2}) are expressed as [24]:

$$i_{xu1} = i_{xd} + 0.5i_x + i_{xr}, \tag{6}$$
$$i_{xu2} = i_{xd} + 0.5i_x - i_{xr}, \tag{7}$$
$$i_{xl1} = i_{xd} - 0.5i_x - i_{xr}, \tag{8}$$
$$i_{xl2} = i_{xd} - 0.5i_x + i_{xr}, \tag{9}$$

where i_{xd}, i_x, and i_{xr} are the DC-circulating current in each leg, the AC output current, and the AC-circulating current, respectively.

The AC output voltage, resonant-frequency voltage and AC output current are:

$$v_{xs} = V_o \sin(\omega t + \delta), \tag{10}$$
$$v_r = V_r \sin(\omega_h t) = 0.25(1-m)V_{dc} \sin(\omega_h t). \tag{11}$$
$$i_x = I_o \sin(\omega t + \delta - \phi), \tag{12}$$

where V_o, V_r and I_o are the voltage and current magnitudes; ω is the fundamental angular frequency; δ is 0, $2\pi/3$, or $-2\pi/3$; ω_h is the resonant angular frequency; m is a modulation index; and ϕ is the phase lag angle. From (2) and (6), the instantaneous power in the top half-arm of the upper arm, p_{xu1}, can be expressed as:

$$p_{xu1} = 0.25V_{dc}i_{xd} - 0.25v_{xs}i_x + 0.125V_{dc}i_x - 0.5v_{xs}i_{xd} - v_r i_{xr}. \tag{13}$$

The first and second terms on the right-hand side of (13) are equal to each other due to the power balance between the DC input side and AC output side. Hence, i_{xd} can be expressed as:

$$i_{xd} = \frac{V_o \sin(\omega t + \delta) \cdot I_o \sin(\omega t + \delta - \phi)}{V_{dc}}. \tag{14}$$

By substituting (10), (12), and (14) into (13),

$$p_{xu1} = 0.125V_{dc}I_o\sin(\omega t+\delta-\phi) - 0.125m^2V_{dc}I_o\sin^2(\omega t+\delta)\sin(\omega t+\delta-\phi) - v_r i_{xr}. \quad (15)$$

In the case of no injection of the resonant-frequency voltage ($v_r i_{xr} = 0$), there are ripple components in the SM capacitor voltage, which is calculated from the half-arm energy variation. By integrating (15), the energy fluctuation in the top half-arm of the upper arm, E_{xu1}, is obtained as:

$$E_{xu1} \approx \frac{V_{dc}I_o}{\omega}\left[\left(0.125-\frac{1}{16}m^2\right)\cos(\omega t+\delta-\phi) + \frac{1}{32}m^2\cos(\omega t+\delta+\phi)\right]. \quad (16)$$

The peak-to-peak voltage ripple of the SM capacitor, ΔV_{c_pp}, is proportional to the variation of the stored energy in half-arm, which can be expressed as:

$$\Delta E_{xu1} = E_{xu1\_\max} - E_{xu1\_\min} = \frac{N}{2}CV_C\Delta V_{C\_pp}, \quad (17)$$

where V_c is the average voltage of the SM capacitor, and E_{xu1_max} and E_{xu1_min} are the maximum and minimum energy during operation, respectively. Then, ΔV_{c_pp} is obtained as follows (see the appendix):

$$\Delta V_{C\_pp} \approx \frac{4I_o}{\omega C}\sqrt{e_1^2+e_2^2}. \quad (18)$$

The SM capacitor voltage ripple is proportional to the output current level and inversely proportional to the fundamental frequency.

The voltage ripples can be suppressed by injecting the resonant-frequency voltage (v_r). In (15), the interaction between the resonant-frequency voltage (v_r) and AC-circulating current (i_{xr}) generates constant power and resonant-frequency power components. The constant power component suppresses the low-frequency power fluctuation (the first and second terms on the right-hand side), so there are only resonant-frequency power components in each half-arm. The power imbalance between the upper and lower arms is redistributed through the flying capacitor by the AC-circulating current. Therefore, the SM capacitor voltage also fluctuates at high frequency, resulting in low voltage ripples [24].

III. DETERMINATION OF RESONANT FREQUENCY AND ADJUSTMENT OF POWER DISTRIBTION THROUGH FLYING-CAPACITOR BRANCH

A. ANALYSIS OF FLYING CAPACITOR VOLTAGE RIPPLES

In order to suppress the SM capacitor voltage ripples, the AC-circulating current, i_{xr}, is controlled to follow the reference, i_{xr}^*, which is given as [24]

$$i_{xr}^* = \frac{I_o\sin(\omega t+\delta-\phi)}{2(1-m)}fcn(f_r,t), \quad (19)$$

where $fcn(f_r, t)$ is of a square waveform expressed as

$$fcn(f_r,t) = \begin{cases} 1, & (0 < t < \frac{1}{2f_r}) \\ -1, & (\frac{1}{2f_r} < t < \frac{1}{f_r}). \end{cases} \quad (20)$$

Based on the AC-circulating current, the flying-capacitor voltage of C_F can be expressed as:

$$v_{CF} = \frac{1}{C_F}\int 2i_{xr}^* dt + \frac{V_{dc}}{2}. \quad (21)$$

Then, the flying-capacitor voltage ripple Δv_{Cf_pp} can be obtained (see the appendix):

$$\Delta v_{CF\_pp} \approx \frac{2I_o}{C_F(1-m)\pi^2}\left[\frac{\sin(\omega_r t+\omega t+\delta-\phi)}{f_r+f} - \frac{\sin(\omega_r t-\omega t-\delta+\phi)}{f_r-f}\right]. \quad (22)$$

To calculate the maximum ripple of the flying-capacitor voltage, $\Delta v_{CF\_pp\_max}$, the low-frequency power fluctuation should be fully canceled out at zero-speed operation ($m = 0$). Hence, $\Delta v_{CF\_pp\_max}$ is obtained as:

$$\Delta v_{CF\_pp\_\max} \approx \frac{4I_o}{\pi^2 C_F f_r}. \quad (23)$$

During the steady state operation of the FC-MMC, the AC-circulating current, i_{xr}, is controlled to flow through the flying capacitor, C_F, in order to redistribute the power difference between the upper and lower arms. It leads to the voltage fluctuation on the flying capacitor around its nominal value. Therefore, it is necessary to maintain the flying-capacitor voltage fluctuation in the limits (±10% of the nominal voltage). In the FC-MMC topology, the nominal voltage of the flying capacitor is a half of V_{dc} [24]; thus, the limits of the peak-to-peak voltage of C_F is 20% of $0.5V_{dc}$, which is expressed as:

$$\Delta v_{CF\_pp\_\max} \le 0.1V_{dc}. \quad (24)$$

Substituting (1) into (23) and (24) yields:

$$f_r \le \frac{V_{dc}}{160I_oL}. \quad (25)$$

With given parameters, the range of f_r can be obtained to maintain Δv_{cF_pp} within the allowable region (0.1 V_{dc}).

B. DETERMINATION OF RESONANT FREQUENCY F_R

As f_r increases, the half-arm power fluctuates at higher frequency. Thus, the SM capacitor is charged and discharged in a shorter period, and the voltage ripple becomes lower. However, in a practical system, f_r should not be too high due to the stability of the system. The flying capacitor voltage ripple is also affected, as mentioned above. Hence, there are some conditions that should be considered to determine f_r:

1) f_r should be low enough to avoid high impedance of equivalent the LC circuit at harmonic frequencies (odd-order harmonics). This means that if f_r is high, the harmonics of the square-wave current cannot flow

through the LC circuit easily. Therefore, the desired square waveform of the injected current, i_{xr}^*, may not be obtained.

2) The SM capacitor voltage includes the sideband frequencies of f_o, $2f_o$, $f_r \pm f_o$ and $f_r \pm 2f_o$, so f_r should be at least two times higher than f_o to avoid excessive voltage ripples in the SM capacitor.
3) For a stable operation, the control error in an AC-circulating current should be regulated as low as possible. Its control bandwidth is usually selected lower than one-fifth of the switching frequency, which is equal to $0.2f_c$ [13], [27]. In this case, the upper limit of resonant frequency becomes $0.1f_c$ according to the Nyquist sampling theorem.
4) To maintain the flying-capacitor voltage ripple within the limit, the resonant frequency, f_r, should be selected according to (25).

Based on the first three conditions, the lower and upper limits of f_r are $2f_o$ and $f_c/10$, respectively. However, f_o varies from zero to the rated fundamental frequency. According to (18), the SM capacitor voltage ripple becomes lower as the operating speed increases. Hence, $f_{threshold}$ is considered as a frequency at which ΔV_{c_pp} fluctuates within the limit. Therefore, the lower limit of f_r is given by

$$2f_{threshold} \leq f_r. \tag{26}$$

Finally, the range of resonant frequency is obtained as

$$2f_{threshold} \leq f_r \leq \min\left\{\frac{V_{dc}}{160I_oL}, 0.1f_c\right\}. \tag{27}$$

TABLE 1. Circuit parameters and rating used for simulation.

Parameters	Symbol	SI	p.u.
Converter			
Apparent power	S	1081 (kVA)	1.0
DC link voltage	V_{dc}	7000 (V)	1.68
Number of SMs per arm	N	4	–
Half-arm inductance	L	2.5 (mH)	0.049
SM DC voltage	v_C^*	1750 (V)	0.42
SM capacitance	C	2300 (μF)	11.5
Defined peak-to-peak voltage ripple of SM	$\Delta v_{c\_pp}^{de}$	260 (V)	0.063
Flying capacitance	C_F	1700 (μF)	8.5
Carrier frequency	f_c	4000 (Hz)	80
Injected resonant frequency	f_r	77.2 (Hz)	1.54
Induction motor			
Output power	P_o	1250 hp	0.87
Rated voltage	V_{LL}	4160 V	1.0
Rated current	I_{rated}	150 A	1.0
Rated frequency	f_o	50 Hz	1.0
Rated speed	ω_{rm_rated}	1470 rpm	1.0
Rated torque	T_{rated}	5970 N.m	1.0

As an example, $f_{threshold}$ is calculated as 12.05 Hz according to (18) with the circuit parameters used for simulations in Table 1. Then, the limit of f_r is 24.1 Hz $< f_r <$ 400 Hz. In addition, based on (25), the region of f_r is obtained as (-∞; 82.5 Hz). f_r should be higher than 0 Hz, so combined with the other limit, the range of f_r is [24.1 Hz $\leq f_r \leq$ 82.5 Hz]. If f_r is set lower than 24.1 Hz, the flying-capacitor voltage ripple Δv_{cF_pp} will be low. However, the SM capacitor voltage ΔV_{c_pp} will fluctuate with high amplitude, so the performance of the converter will not be good. If f_r is higher than 82.5 Hz, Δv_{CF_pp} will exceed the maximum range ($0.1V_{dc}$). Therefore, f_r is set as 77.2 Hz in the simulation. Similarly, f_r is chosen as 46.4 Hz for the experimental parameters listed in Table 2.

TABLE 2. Performance comparison between the proposed and conventional methods.

	[24]	[26]	Proposed
[a] Peak value of AC-circulating current (i_{xr})	1.870	1.100	0.727
[a] Peak value of half-arm currents ($i_{xu/l1\ or\ 2}$)	2.600	2.000	1.733
[a] Peak-to-peak value of flying capacitor voltage (Δv_{CF})	0.359	0.325	0.156

[a]The unit is p.u.

C. ADJUSTMENT OF POWER DISTRIBTION THROUGH FLYING-CAPACITOR BRANCH FOR CURRENT STRESS REDUCTION

As seen in (15), the low-frequency power fluctuation is completely cancelled out by $v_r i_{xr}$, so an injected current (i_{xr}) with high amplitude flows through the flying-capacitors and switching devices. Thus, the amplitude of i_{xr} can be reduced by controlling $v_r i_{xr}$ to follow the reference $v_r^* i_{xr}^*$, which is expressed as:

$$\begin{aligned} v_r^* i_{xr}^* = k(&0.125V_{dc}I_o\sin(\omega t+\delta-\phi) \\ &-0.125V_{dc}m^2I_o\sin^2(\omega t+\delta)\sin(\omega t+\delta-\phi)), \end{aligned} \tag{28}$$

where k is a factor which is used to regulate the low-frequency power fluctuation to be cancelled out and its range is from 0 to 1. The reference of the square-wave voltage to be injected, v_r^*, is expressed as

$$v_r^* = V_r^* fcn(f_r, t) = \begin{cases} V_r^*, & (0 < t < \dfrac{1}{2f_r}) \\ -V_r^*, & (\dfrac{1}{2f_r} < t < \dfrac{1}{f_r}). \end{cases} \tag{29}$$

If $k = 1$, the low-frequency power fluctuation is compensated completely, and if $k = 0$, there are no injections of v_r^* and i_{xr}^*. Then, substituting (28) into (15), p_{xu1} can be obtained as:

$$\begin{aligned} p_{xu1} = (1-k)(&0.125V_{dc}I_o\sin(\omega t+\delta-\phi) \\ &-0.125V_{dc}m^2I_o\sin^2(\omega t+\delta)\sin(\omega t+\delta-\phi)). \end{aligned} \tag{30}$$

By integrating (30), the energy fluctuation in the top half-arm of the upper arm, E_{xu1}, is derived again as:

$$\begin{aligned} E_{xu1} \approx (1-k)\frac{V_{dc}I_o}{\omega}\Bigg[&\left(0.125-\frac{1}{16}m^2\right)\cos(\omega t+\delta-\phi) \\ &+\frac{1}{32}m^2\cos(\omega t+\delta+\phi)\Bigg]. \end{aligned} \tag{31}$$

The energy fluctuation, ΔE_{xu1}, is:

$$\Delta E_{xu1} = E_{xu1\_\max} - E_{xu1\_\min} = (1-k)\frac{2V_{dc}I_o}{\omega}\sqrt{e_1^2+e_2^2}. \tag{32}$$

Together with the specified voltage fluctuation limit, $\Delta V_{c\_pp\_de}$, the variation of stored energy in half-arm in (17) is derived:

$$\Delta E_{xu1} = \frac{N}{2} C V_C \Delta V_{C\_pp\_de}. \tag{33}$$

From (32) and (33), the value of k can be obtained:

$$k = 1 - \frac{\omega C \Delta V_{C\_pp\_de}}{4I_o\sqrt{e_1^2+e_2^2}}. \tag{34}$$

At very low speeds, k is nearly equal to one. Thus, the proposed method is similar to a conventional method [24], and the amplitude of i_{xr} is not much different. When the operating speed is higher, k becomes lower. This implies that less power redistribution through the flying-capacitor required to force the SM capacitor voltage ripple to be within $\Delta V_{c\_pp\_de}$. Thus, the amplitude of i_{xr} is reduced. During operation, k is also increased when a load is applied.

To maintain the SM capacitor voltage ripples within $\Delta V_{c\_pp\_de}$, the AC-circulating current, i_{xr}, in (6)-(9), should be controlled to follow the reference i_{xr}^*, which is obtained by inserting (29) into (28):

$$\begin{aligned} i_{xr}^* &= I_{xr}^* fcn(f_r, t) \\ &\approx k\frac{I_o(2-m^2)\sin(\omega t+\delta-\phi)}{4(1-m)} fcn(f_r, t). \end{aligned} \tag{35}$$

D. CONTROL ALGORITHM

Block diagrams of the proposed control strategy are shown in Fig. 2 with an averaging control scheme [6] in Fig. 2(a) and a half-arm balancing control scheme [24] in Fig. 2(b). In the averaging control, v_C^* and $\Delta v_{ph,x}^*$ are the SM capacitor voltage reference and compensating phase voltage command, respectively. The average SM capacitor voltage in each leg, $\bar{v}_{Cx}$, is expressed as:

$$\bar{v}_{Cx} = \frac{1}{2N}\sum_{j=1}^{2N} v_{Cj,x}, \tag{36}$$

where $v_{Cj,x}$ is the feedback signal of the SM capacitor voltage. In the half-arm balancing control, the average SM capacitor voltage in each half-arm is calculated as:

$$v_{xu/l1,2}^{avg} = \frac{1}{0.5N}\sum_{j=1}^{0.5N} v_{Cj,x}. \tag{37}$$

Then, the output of the half-arm balancing control is the compensating half-arm voltage command $\Delta v_{xu/l}^*$.

Fig. 2(c) shows a block diagram of the AC-circulating current controller, which forces i_{xr} to follow i_{xr}^* as expressed in (35). This controller includes only the current controller, which is different from the arm capacitor voltage control, which consists of an outer voltage and inner current control loop [24]. With only the current controller, the SM capacitor voltage ripples are maintained within the specified $\Delta V_{c\_pp\_de}$ instead of being completely eliminated. The output of the controller is the voltage command, Δv_{xr}^*.

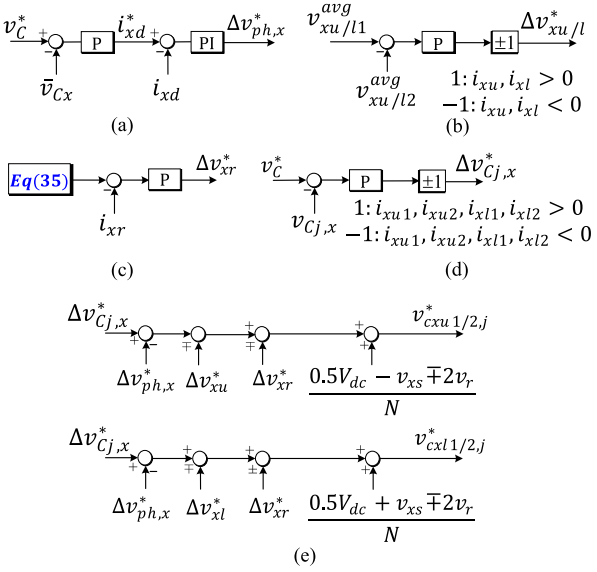

FIGURE 2. Block diagrams for the proposed control strategy. (a) Averaging control. (b) Half-arm balancing control. (c) AC-circulating current control. (d) Individual SM balancing control. (e) SM voltage reference generation.

The individual SM balancing control is illustrated in Fig. 2(d). The voltage references of SMs, $v_{Cxu1/2,j}^*$ and $v_{Cxl1/2,j}^*$, are synthesized in Fig. 2(e). Finally, they are normalized by v_C^* and sent to a PWM generator.

IV. SIMULATION RESULTS

The validity of the proposed control strategy is verified by simulation results for a 4160-V/1-MW FC-MMC system with four SMs per arm. In Table 1, the parameters of the converter and induction motor are listed. To verify the effectiveness of the proposed method, the conventional method [24] is considered together, which has been previously applied to the induction motor drive system.

In the FC-MMC, there is a trade-off between the current stress and capacitor cost. The minimum capacitance of SM capacitor, which can be calculated, is 802 μF and the flying capacitor is 1500 μF [28]. It results in 54.4 ms of an energy storage constant, H [29]. With this minimum capacitance of SM capacitor, under full load condition and low-speed operation, the low-frequency power fluctuation should be cancelled out completely ($k = 1$); thus, the performance of proposed method is similar to that of the conventional method [24]. It means that the advantage of the proposed method for reduction of current stresses is effective only under light load conditions. In order to utilize the superiority of the proposed method under full load condition, the SM capacitance is designed with larger value, which is 2300 μF; besides, the flying capacitance is 1700 μF. Based on those

selected values, the energy storage constant, H, is calculated as 107 ms.

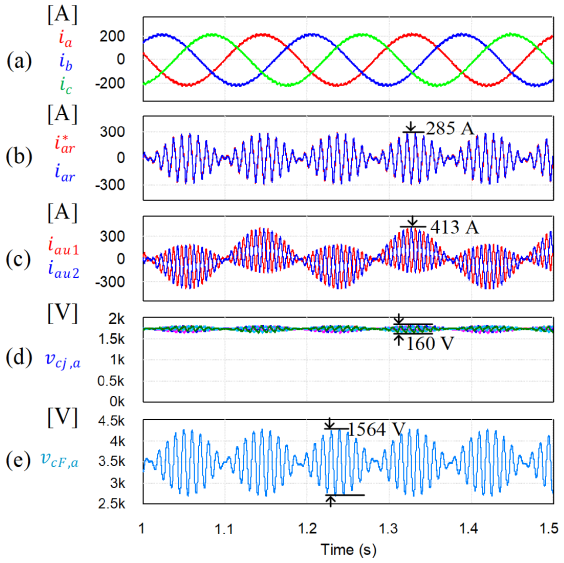

FIGURE 3. Performance of the conventional method. (a) Three-phase output current. (b) AC-circulating current. (c) Top and bottom half-arm currents in the upper arm. (d) SM capacitor voltages of phase-*a*. (e) Flying capacitor voltage in phase-*a*.

Fig. 3 shows the performance of the FC-MMC with the conventional method [24] at $\omega_{rm} = 150$ rpm under full load condition. A sinusoidal waveform is used in the injected voltage and current (v_r and i_{xr}). The three-phase output current waveform is illustrated in Fig. 3(a), where the RMS value is 150 A. The AC-circulating current i_{ar} follows the reference i^*_{ar} well with a peak value of 285 A, as shown in Fig. 3(b). Fig. 3(c) shows the waveform of the top and bottom half-arm currents in the upper arm with a peak value of 413 A. The currents include the resonant frequency component, which allows the power difference to be redistributed between the upper and lower arms through the flying capacitor. Therefore, the SM capacitor voltage ripple, ΔV_{c_pp}, is suppressed as 160 V (9% of 1750-V base), as shown in Fig. 3(d). According to (18), the SM capacitor voltage ripple without injecting resonant-frequency components is calculated as 1487 V. Hence, ΔV_{c_pp} is mitigated significantly in the FC-MMC. However, the flying capacitor current (double the value of i_{xr}) leads to ripple of the flying capacitor voltage, which is 1564 V (44.7% of the 3500-V base), as shown in Fig. 3(e). This value exceeds the maximum flying capacitor voltage limit ($0.1V_{dc} = 700$ V). The power difference between the upper and lower arms is fully redistributed, so the value of k can be considered as one in the conventional method.

Fig. 4 shows the performance of the FC-MMC with the proposed control scheme at $\omega_{rm} = 150$ rpm under full load condition with $\Delta V_{c\_pp\_de}$ set as 260 V. The three-phase output current waveform is shown in Fig. 4(a) with the same RMS value as in Fig. 3(a). The AC-circulating current reference, i^*_{ar}, is controlled in the shape of square wave, as illustrated

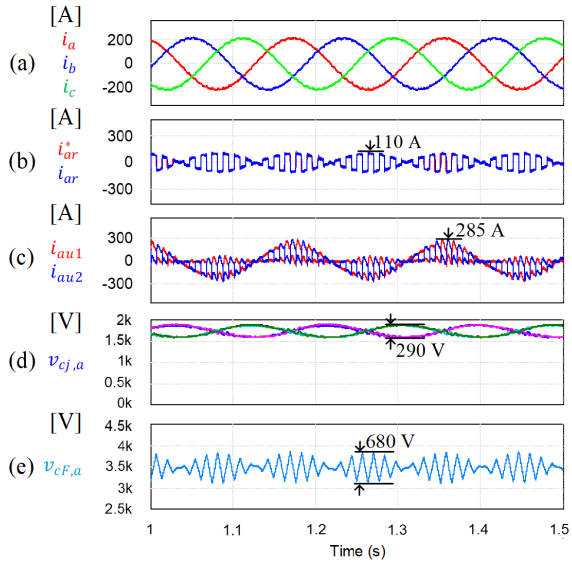

FIGURE 4. Performance of proposed control scheme. (a) Three-phase output current. (b) AC-circulating current. (c) Top and bottom half-arm currents in the upper arm. (d) SM capacitor voltages of phase-*a*. (e) Flying capacitor voltage in phase-*a*.

in Fig. 4(b). The AC-circulating current, i_{ar}, can well track its reference with the appropriate resonant frequency (77.2 Hz), of which peak value is 110 A. Fig. 4(c) shows the top and bottom half-arm currents in the upper arm with 285 A peak value. Compared with the method of [24], the AC-circulating current and the half-arm currents with the proposed method are reduced by 61.4% and 30%, respectively. The SM capacitor voltage ripples in Fig. 4(d) are 290 V (17% of the 1750-V base), which are kept within the allowable range. The power difference between the upper and lower arms is not fully redistributed as in the conventional method, so k is 0.82. Fig. 4(e) shows the flying capacitor voltage, where the ripple is low (680 V) compared to that of the conventional one (1496 V) and does not exceed the maximum voltage limit ($0.1V_{dc}$).

Fig. 5 illustrates the performance of the proposed control scheme at low-speed operation ($\omega_{rm} = 150$ rpm) when the load torque is changed from no load to full load and back to no load at $t = t_1$. Figs. 5(a) – (c) show the three-phase output current, the AC-circulating current, and the top and bottom half-arm currents in the upper arm, respectively. During operation, the SM capacitor voltages are kept within the specified $\Delta V_{c\_pp\_de}$ (290 V), which is illustrated in Fig. 5(d). According to (34), k increases as the load is increased. Hence, k changes from 0.46 to 0.82 at $t = t_0$. The voltage ripple in flying capacitor is demonstrated in Fig. 5(f), where the maximum peak-to-peak value at the rated load is 680 V (19.4% of 3500-V base).

Fig. 6 shows the performance of the acceleration operation in no-load condition. The motor speed, ω_{rm}, is increased from zero at $t = t_0$ to the rated speed of 1470 rpm, as shown in Fig. 6(a). The phase output voltage and the three-phase output current are shown in Figs. 6(b) and (c), respectively,

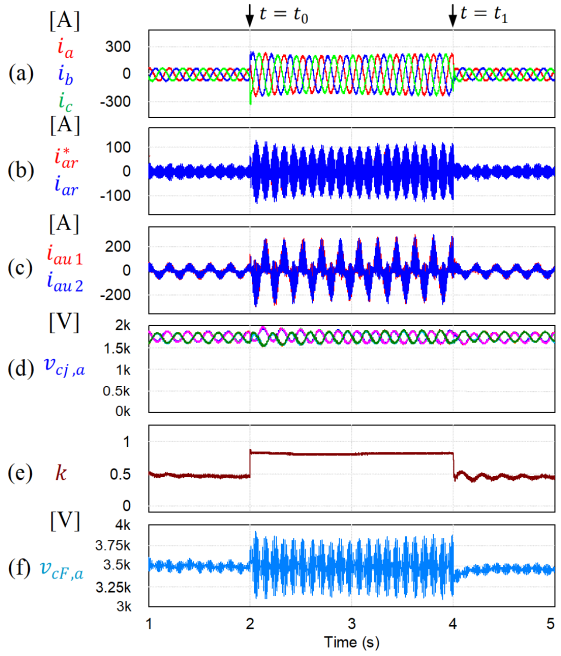

FIGURE 5. Performance of proposed control scheme at $\omega_{rm} = 150$ rpm under load change. (a) Three-phase output current. (b) AC-circulating current. (c) Top and bottom half-arm currents in the upper arm. (d) SM capacitor voltages of phase-*a*. (e) Factor *k*. (f) Flying-capacitor voltage in phase-*a*.

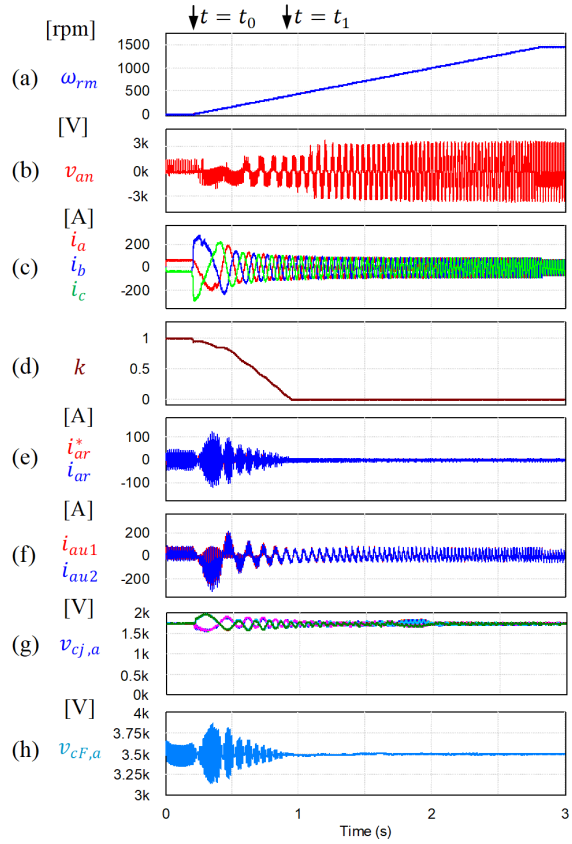

FIGURE 6. Performance accelerating process from zero to rated speed under no load. (a) Motor mechanical speed. (b) Phase output voltage. (c) Three-phase output current. (d) Factor *k*. (e) AC-circulating current. (f) Top and bottom half-arm currents in the upper arm. (g) SM capacitor voltages of phase-*a*. (h) Flying capacitor voltage in phase-*a*.

where their fundamental frequency is increased gradually from 0 to 50 Hz. Fig. 6(d) shows the factor k. According to (34), k is equal to one initially at $t = t_0$. As the motor speed increases, k decreases gradually to zero at $t = t_1$. Thus, the operating speed is high enough for the SM capacitor voltages to be naturally balanced and maintained within acceptable limit without the AC-circulating current, i_{ar}, flowing through the flying capacitor. Hence, the AC-circulating current, i_{ar}, becomes zero at $t = t_1$, as shown in Fig. 6(e). The top and bottom half-arm currents in the upper arm are shown in Fig. 6(f). The SM capacitor voltages and the flying-capacitor voltages are illustrated in Figs. 6(g) and (h), where the ripples become low at high-speed region.

Table 2 summarizes the control performances of the proposed and conventional methods, where the RL (0.9 Ω; 10 mH; Y-connection) load is applied. With the proposed method, the peak value of half-arm currents ($i_{xu/l1or2}$) is reduced by 33.3% and 13.3%, respectively, compared with [24] and [26]. It leads to the reduction of the current stress on switching devices. Furthermore, the peak value of AC-circulating current (i_{xr}) is reduced by 61.1% and 34%, respectively, which also results in lower current stress on flying capacitors. In addition, in the proposed method, the peak-to-peak value of flying capacitor voltage (Δv_{CF}) is maintained within an allowable range (0.168 p.u.; 700 V).

V. EXPERIMENTAL RESULTS

The proposed method was also validated by experimental tests with a FC-MMC that has four SMs per arm. The DC-link

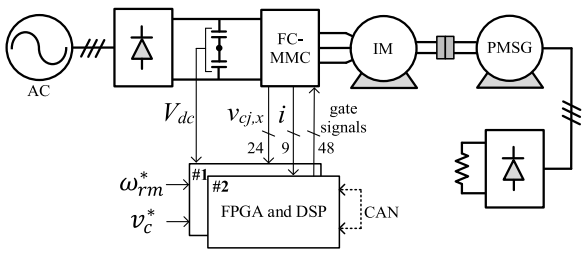

FIGURE 7. Experimental system configuration.

voltage is 300 V, and the capacitor voltage reference, v_C^*, is 75 V. Fig. 7 shows the experimental system configuration, where a 230-V/3-kW induction motor is coupled with a PMSG to apply the load. The DC-link voltage, V_{dc}, the 24 SM capacitor voltages, $v_{Cx,j}$, and the 12 half-arm currents are sent to two main controllers, which consist of an FPGA (Xilinx XC3S400) and DSP (TMS320F28335). CAN communication is used to transfer data between these controllers. Comparisons are made between the SM voltage references, $v^*_{Cxu/l12,j}$, and the corresponding triangular carrier signals, and then 48 gate signals are produced and sent to the SMs of the converter. The field-oriented control is applied to

the speed control of the induction motor drive. In Table 3, the specifications of the converter and induction motor for the experiment are listed. A photo of the prototype setup is shown in Fig. 8.

TABLE 3. Induction motor parameters and ratings.

Parameters	Symbol	SI	p.u.
Converter			
Apparent power	S	3.57 (kVA)	1
DC link voltage	V_{dc}	300 (V)	1.3
Number of SMs per arm	N	4	–
Half-arm inductance	L	2.5 (mH)	0.053
SM DC voltage	v_C^*	75 (V)	0.35
SM capacitance	C	3800 (μF)	17.6
Defined peak-to-peak voltage ripple of SM	$\Delta v_{c\_pp}^{de}$	12 (V)	0.052
Flying capacitance	C_F	4700 (μF)	21.8
Carrier frequency	f_c	4000 (Hz)	80
Injected Resonant frequency	f_r	46.4 (Hz)	0.93
Induction motor			
Output power	P_o	4 hp	0.84
Rated voltage	V_{LL}	230 V	1
Rated current	I_{rated}	10.9 A	1.2
Rated frequency	f_o	50 Hz	1
Rated speed	ω_{rm_rated}	1430 rpm	1
Rated torque	T_{rated}	19 N.m	1

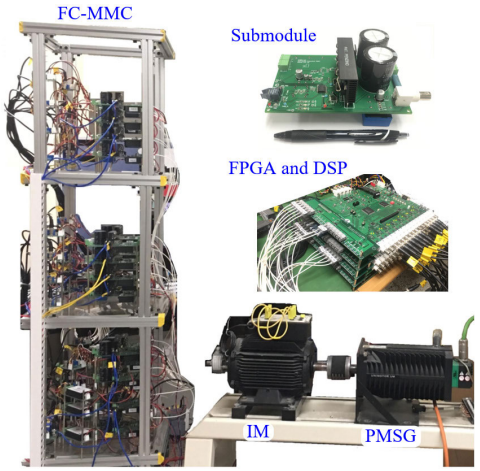

FIGURE 8. Experimental prototype of FC-MMC and induction motor.

Fig. 9 demonstrates the performance of the FC-MMC with the conventional method [24] at $\omega_{rm} = 150$ rpm under full load condition. The three-phase output current waveform is shown in Fig. 9(a), where the RMS value is 10.9 A. The AC-circulating current is demonstrated in Fig. 9(b) with a peak value of 19.5 A. The top and bottom half-arm currents in the upper arm are shown in Fig. 9(c) with a peak value of 27.5 A. Due to the power difference redistribution between the upper and lower arms through the flying capacitor, the SM capacitor voltage ripple, ΔV_{c_pp}, is suppressed around 9 V (12% of 75-V base), as shown in Fig. 9(d). Fig. 9(e) illustrates the ripple of the flying capacitor voltage which is around 93 V (62% of 150-V base). This value is higher than the maximum flying capacitor voltage limit ($0.1V_{dc} = 30$ V).

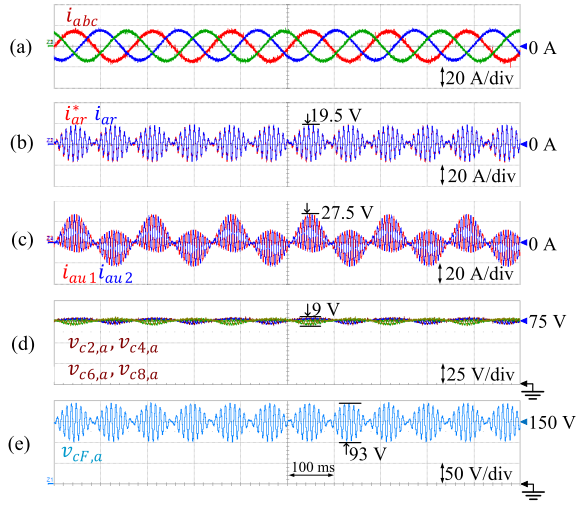

FIGURE 9. Performance of the conventional method. (a) Three-phase output current. (b) AC-circulating current. (c) Top and bottom half-arm currents in the upper arm. (d) SM capacitor voltages of phase-*a*. (e) Flying capacitor voltage in phase-*a*.

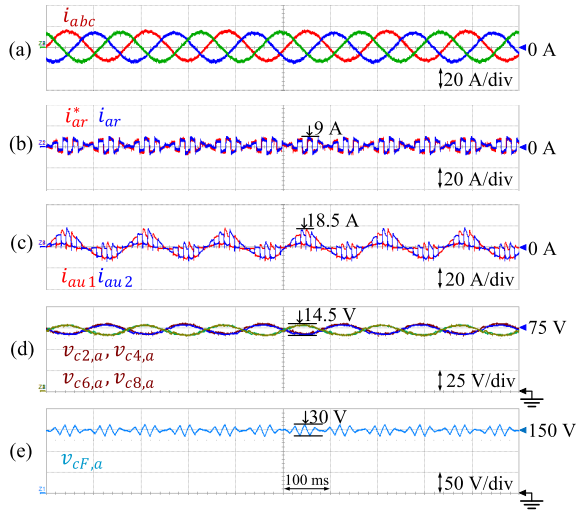

FIGURE 10. Performance of proposed control scheme. (a) Three-phase output current. (b) AC-circulating current. (c) Top and bottom half-arm currents in the upper arm. (d) SM capacitor voltages of phase-*a*. (e) Flying capacitor voltage in phase-*a*.

Fig. 10 shows the performance of the FC-MMC with the proposed control scheme, where $\Delta V_{c\_pp\_de}$ is set as 16% of v_C^* (12 V). During operation, k is 0.82. The three-phase output current is shown in Fig. 10(a) with an RMS value of 10.9 A. Fig. 10(b) illustrates the performance of the AC-circulating current controller. It shows that the AC-circulating current can follow the square-wave of current reference well with the resonant frequency value of 46.4 Hz, and its peak value is 9 A. Fig. 10(c) shows the top and bottom half-arm currents in the upper arm with a peak value of 18.5 A. The SM capacitor voltage ripples in Fig. 10(d) are 14.5 V (19.3% of the 75-V base), which are maintained within the allowable range. As a result of neglecting the minor terms in (13), the result is slightly different from the defined value of

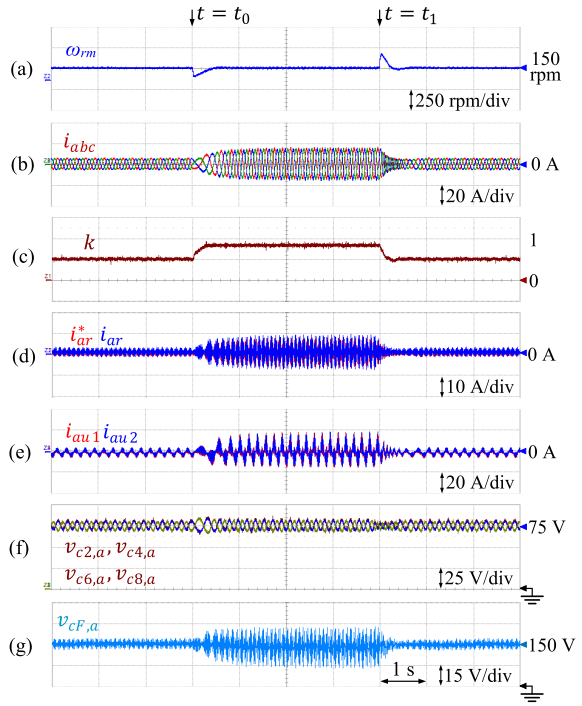

FIGURE 11. Performance of proposed control scheme at $\omega_{rm} = 150$ rpm under load change. (a) Motor mechanical speed. (b) Three-phase output current. (c) Factor k. (d) AC-circulating current. (e) Top and bottom half-arm currents in the upper arm. (f) SM capacitor voltages of phase-a. (g) Flying-capacitor voltage in phase-a.

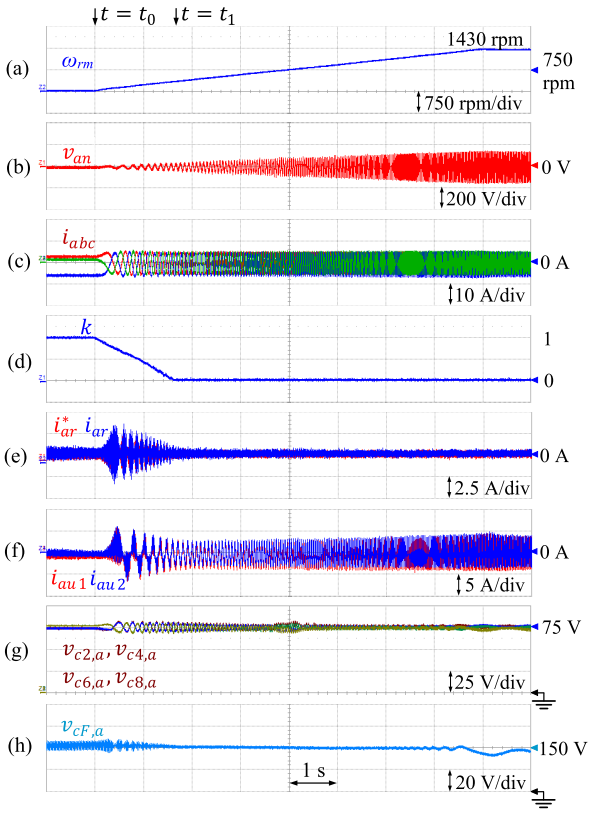

FIGURE 12. Performance accelerating process from zero to rated speed under no load. (a) Motor mechanical speed. (b) Phase output voltage. (c) Three-phase output current. (d) Factor k. (e) AC-circulating current. (f) Top and bottom half-arm currents in the upper arm. (g) SM capacitor voltages of phase-a. (h) Flying capacitor voltage in phase-a.

$\Delta V_{c\_pp\_de}$ (12 V). Compared with the method [24], which is shown in Fig. 9, the AC-circulating and half-arm currents are decreased by 53.8% and 32.7%, respectively. It leads to the reduction of current stresses on the switching devices, inductors and flying capacitors. Fig. 10(e) demonstrates the flying capacitor voltage in phase-a, v_{CFa}, where the ripple is low (30 V) compared to that of the conventional method (93 V) and it does not exceed the maximum voltage limit ($0.1V_{dc}$). Thus, by selecting appropriately the frequency limit of the circulating current, the flying-capacitor voltage ripple can be kept within the acceptable range.

Fig. 11 illustrates the performance of the proposed control scheme at low-speed operation ($\omega_{rm} = 150$ rpm) under changing load. The load torque is changed from no load to full load at $t = t_0$ and back to no load at $t = t_1$. The motor speed and the three-phase output current are shown in Figs. 11(a) and (b), respectively. In Fig. 11(c), k is equal to 0.5 at no load, while it is 0.82 at full load. The AC-circulating current and the top and bottom half-arm currents in the upper arm are shown in Fig. 11(d) and (e), respectively. The SM capacitor voltages of phase-a (v_{c2a}, v_{c4a}, v_{c6a} and v_{c8a}) and the flying capacitor voltage are shown in Fig. 11(f) and (g), respectively.

Fig. 12 shows the performance of the acceleration operation at no load. In Fig. 12(a), the motor speed, ω_{rm}, is increased from zero at $t = t_0$ to the rated speed of 1430 rpm without overshoot or undershoot. The phase output voltage and three-phase output current are shown in Figs. 12(b) and (c). In Fig. 12(d), k is high to maintain the SM capacitor voltage within the limit at low speed. k becomes zero at $t = t_1$. The operating speed is high enough for the SM capacitor voltages to be naturally balanced without power redistribution between the upper and lower arms. Thus, the AC-circulating current, i_{ar}, reaches to zero at $t = t_1$, as shown in Fig. 12(e). The top and bottom half-arm currents in the upper arm are shown in Fig. 12(f). The SM capacitor voltage and flying capacitor voltage are demonstrated in Fig. 12(g) and (h), respectively. The maximum peak-to-peak AC voltage fluctuation of SM capacitor is 14.5 V, which is 19.3% of 75 V.

VI. CONCLUSION

This paper has proposed a control method which is able to reduce the peak value of half-arm currents and flying capacitor voltage ripples for a FC-MMC. Specifically, how to determine the frequency range of the square-wave voltage to be injected has been suggested, with which the flying-capacitor voltage ripples can be kept within the allowable range and the control performance of the AC-circulating current is improved. By adjusting the power difference between the upper and lower arms through the flying capacitor branch, the current stresses on switching devices and flying capacitors

have been reduced by 53.8% and 32.7%, respectively, for experimental tests. The proposed control algorithm has been implemented for a 4160-V/1-MW simulation model and a 230-V/3-kW prototype of the FC-MMC-fed induction motor drive.

APPENDIX

A. DERIVATION OF (18)

In (16), the energy fluctuation of the top half-arm in the upper arm, E_{xu1}, can be derived as:

$$E_{xu1} \approx \frac{V_{dc}I_o}{\omega}\left[\left(0.125-\frac{3}{32}m^2\right)\cos(\omega t+\delta)\cos(\phi) + \left(0.125-\frac{1}{32}m^2\right)\sin(\omega t+\delta)\sin(\phi)\right]. \quad (38)$$

From (38), the maximum and minimum values are:

$$E_{xu1\_\max} = \frac{V_{dc}I_o}{\omega}\sqrt{e_1^2+e_2^2}, \quad (39)$$

$$E_{xu1\_\min} = -E_{xu1\_\max}, \quad (40)$$

where

$$e_1 = \left(0.125-\frac{3}{32}m^2\right)\cos(\phi), \quad (41)$$

$$e_2 = \left(0.125-\frac{1}{32}m^2\right)\sin(\phi). \quad (42)$$

B. DERIVATION OF (22)

Using Fourier expansion, $fcn(f_r,t)$ is expressed as:

$$fcn(f_r,t) = \frac{4}{\pi}\sum_{n=1,3,5,\ldots}^{\infty}\frac{1}{n}\sin(n.2\pi f_r t). \quad (43)$$

For a simplified derivation, it is assumed that the square-wave function, $fcn(f_r,t)$, consists of only the fundamental frequency with higher order harmonics neglected. Substituting (19) and (43) into (21),

$$v_{CF} = \frac{2}{C_F}\int \frac{I_o\sin(\omega t+\delta-\phi)}{2(1-m)}\cdot\frac{4\sin(\omega_r t)}{\pi}dt + \frac{V_{dc}}{2}. \quad (44)$$

From (44), the flying-capacitor voltage ripple, Δv_{CF_pp}, in (22) is obtained.

REFERENCES

[1] S. Allebrod, R. Hamerski, and R. Marquardt, "New transformerless, scalable modular multilevel converters for HVDC-transmission," in *Proc. IEEE Power Electron. Spec. Conf.*, Jun. 2008, pp. 174–179.

[2] J. Peralta, H. Saad, S. Dennetiere, J. Mahseredjian, and S. Nguefeu, "Detailed and averaged models for a 401-level MMC–HVDC system," *IEEE Trans. Power Del.*, vol. 27, no. 3, pp. 1501–1508, Jul. 2012.

[3] C. Wang, L. Xiao, L. Zhang, F. Wu, and Q. Liu, "Analysis of distortions in switch drives and currents related to balance strategy with sort method in MMC systems," *J. Power Electron.*, vol. 20, no. 2, pp. 399–409, Mar. 2020.

[4] Y.-J. Jo, T. H. Nguyen, and D.-C. Lee, "Capacitance estimation of the submodule capacitors in modular multilevel converters for HVDC applications," *J. Power Electron.*, vol. 16, no. 5, pp. 1752–1762, Sep. 2016.

[5] Q. Zeng, F. Xiao, Q. Ren, and S. Ai, "Modulation signal analysis and parameter selection for modular multi-level converters with harmonic injection method," *J. Power Electron.*, vol. 20, no. 2, pp. 455–465, Mar. 2020.

[6] M. Hagiwara, K. Nishimura, and H. Akagi, "A medium-voltage motor drive with a modular multilevel PWM inverter," *IEEE Trans. Power Electron.*, vol. 25, no. 7, pp. 1786–1799, Jul. 2010.

[7] S. Debnath, J. Qin, and M. Saeedifard, "Control and stability analysis of modular multilevel converter under low-frequency operation," *IEEE Trans. Ind. Electron.*, vol. 62, no. 9, pp. 5329–5339, Sep. 2015.

[8] J.-J. Jung, H.-J. Lee, and S.-K. Sul, "Control strategy for improved dynamic performance of variable-speed drives with modular multilevel converter," *IEEE J. Emerg. Sel. Topics Power Electron.*, vol. 3, no. 2, pp. 371–380, Jun. 2015.

[9] D. D. Le and D.-C. Lee, "A modified hybrid modular multilevel converter with reduced capacitor voltage fluctuations and fault-tolerant operation ability," in *Proc. IEEE ECCE Asia*, May 2019, pp. 172–177.

[10] J. I. Y. Ota, Y. Shibano, N. Niimura, and H. Akagi, "A phase-shifted-PWM D-STATCOM using a modular multilevel cascade converter (SSBC)—Part I: Modeling, analysis, and design of current control," *IEEE Trans. Ind. Appl.*, vol. 51, no. 1, pp. 279–288, Jan. 2015.

[11] J. I. Y. Ota, Y. Shibano, and H. Akagi, "A phase-shifted PWM D-STATCOM using a modular multilevel cascade converter (SSBC)—Part II: Zero-voltage-ride-through capability," *IEEE Trans. Ind. Appl.*, vol. 51, no. 1, pp. 289–296, Jan. 2015.

[12] A. J. Korn, M. Winkelnkemper, and P. Steimer, "Low output frequency operation of the modular multi-level converter," in *Proc. IEEE Energy Convers. Congr. Expo.*, Sep. 2010, pp. 3993–3997.

[13] M. Hagiwara, I. Hasegawa, and H. Akagi, "Start-up and low-speed operation of an electric motor driven by a modular multilevel cascade inverter," *IEEE Trans. Ind. Appl.*, vol. 49, no. 4, pp. 1556–1565, Apr. 2013.

[14] M. Al Sabbagh, H. Rehman, J. Pan, and L. Xu, "Suppressing the capacitor voltage fluctuations in low frequency operation of modular multilevel converters," *IEEE Access*, vol. 8, pp. 46141–46150, 2020.

[15] R. Picas, J. Zaragoza, J. Pou, S. Ceballos, G. Konstantinou, and G. J. Capella, "Study and comparison of discontinuous modulation for modular multilevel converters in motor drive applications," *IEEE Trans. Ind. Electron.*, vol. 66, no. 3, pp. 2376–2386, Mar. 2019.

[16] Y. S. Kumar and G. Poddar, "Control of medium-voltage AC motor drive for wide speed range using modular multilevel converter," *IEEE Trans. Ind. Electron.*, vol. 64, no. 4, pp. 2742–2749, Apr. 2017.

[17] F. Zhao, G. Xiao, T. Zhu, X. Zheng, Z. Wu, and T. Zhao, "A coordinated strategy of low-speed and start-up operation for medium-voltage variable-speed drives with a modular multilevel converter," *IEEE Trans. Power Electron.*, vol. 35, no. 1, pp. 709–724, Jan. 2020.

[18] B. Li, S. Zhou, D. Xu, S. J. Finney, and B. W. Williams, "A hybrid modular multilevel converter for medium-voltage variable-speed motor drives," *IEEE Trans. Power Electron.*, vol. 32, no. 6, pp. 4619–4630, Jun. 2017.

[19] A. Antonopoulos, L. Ängquist, and H.-P. Nee, "On dynamics and voltage control of the modular multilevel converter," in *Proc. 13th ECPE Eur.*, Sep. 2009, pp. 1–10.

[20] A. Antonopoulos, L. Angquist, L. Harnefors, and H.-P. Nee, "Optimal selection of the average capacitor voltage for variable-speed drives with modular multilevel converters," *IEEE Trans. Power Electron.*, vol. 30, no. 1, pp. 227–234, Jan. 2015.

[21] A. Antonopoulos, L. Angquist, S. Norrga, K. Ilves, L. Harnefors, and H.-P. Nee, "Modular multilevel converter AC motor drives with constant torque from zero to nominal speed," *IEEE Trans. Ind. Appl.*, vol. 50, no. 3, pp. 1982–1993, May 2014.

[22] B. Li, S. Zhou, D. Xu, R. Yang, D. Xu, C. Buccella, and C. Cecati, "An improved circulating current injection method for modular multilevel converters in variable-speed drives," *IEEE Trans. Ind. Electron.*, vol. 63, no. 11, pp. 7215–7225, Nov. 2016.

[23] M. Huang, J. Zou, and X. Ma, "Hybrid modular multilevel converter with redistributed power to reduce submodule capacitor voltage fluctuation," *IEEE Trans. Power Electron.*, vol. 33, no. 8, pp. 6595–6607, Aug. 2018.

[24] S. Du, B. Wu, N. R. Zargari, and Z. Cheng, "A flying-capacitor modular multilevel converter for medium-voltage motor drive," *IEEE Trans. Power Electron.*, vol. 32, no. 3, pp. 2081–2089, Mar. 2017.

[25] D. D. Le, D.-C. Lee, and H.-G. Kim, "Three-phase flying-capacitor MMC with six coupled inductors," *J. Power Electron.*, vol. 20, no. 4, pp. 916–925, Jul. 2020.

[26] S. Du, B. Wu, and N. R. Zargari, "Current stress reduction for flying-capacitor modular multilevel converter," *IEEE Trans. Power Electron.*, vol. 34, no. 1, pp. 184–191, Jan. 2019.

[27] M. Monfared, S. Golestan, and J. M. Guerrero, "Analysis, design, and experimental verification of a synchronous reference frame voltage control for single-phase inverters," *IEEE Trans. Ind. Electron.*, vol. 61, no. 1, pp. 258–269, Jan. 2014.
[28] K. Ilves, S. Norrga, L. Harnefors, and H.-P. Nee, "On energy storage requirements in modular multilevel converters," *IEEE Trans. Power Electron.*, vol. 29, no. 1, pp. 77–88, Jan. 2014.
[29] M. Hagiwara and H. Akagi, "Control and experiment of pulsewidth-modulated modular multilevel converters," *IEEE Trans. Power Electron.*, vol. 24, no. 7, pp. 1737–1746, Jul. 2009.

DUC DUNG LE (Student Member, IEEE) received the B.S. degree in electrical engineering from the Ho Chi Minh City University of Technology, Ho Chi Minh City, Vietnam, in 2013. He is currently pursuing the Ph.D. degree with the Department of Electrical Engineering, Yeungnam University, Gyeongsan, South Korea. His current research interests include multi-level converters and DC microgrids.

DONG-CHOON LEE (Senior Member, IEEE) received the B.S., M.S., and Ph.D. degrees in electrical engineering from Seoul National University, Seoul, South Korea, in 1985, 1987, and 1993, respectively.

He was a Research Engineer with Daewoo Heavy Industry, South Korea, from 1987 to 1988. He has been a Faculty Member with the Department of Electrical Engineering, Yeungnam University, Gyeongsan, South Korea, since 1994. He was a Visiting Scholar with the Power Quality Laboratory, Texas A&M University, College Station, TX, USA, in 1998; the Electrical Drive Center, University of Nottingham, Nottingham, U.K., in 2001; the Wisconsin Electric Machines and Power Electronics Consortium, University of Wisconsin, Madison, WI, USA, in 2004; and the FREEDM Systems Center, North Carolina State University, Raleigh, NC, USA, from September 2011 to August 2012. His current research interests include power converter design and control, renewable energy and its grid connection, AC machine drives, and DC power system. He has served as the Editor-in-Chief of the *Journal of Power Electronics* of the Korean Institute of Power Electronics (KIPE) from January 2015 to December 2017, where he has served as the President in 2019.